Damage Evolution in Composites with a Homogenization-based Continuum Damage Mechanics Model

JAYESH R. JAIN AND SOMNATH GHOSH*

Computational Mechanics Research Laboratory
Department of Mechanical Engineering
The Ohio State University, Columbus, OH 43210, USA

ABSTRACT: This paper develops a 3D homogenization-based continuum damage mechanics (HCDM) model for fiber reinforced composites undergoing micromechanical damage. Micromechanical damage in the representative volume element (RVE) is explicitly incorporated in the form of fiber–matrix interfacial debonding. The model uses the evolving principal damage coordinate system as its reference in order to represent the anisotropic coefficients. This is necessary for retaining accuracy with nonproportional loading. The material constitutive law involves a fourth order orthotropic tensor with stiffness characterized as macroscopic internal variable. Damage in 3D composites is accounted for through functional forms of the fourth order damage tensor in terms of macroscopic strain components. The HCDM model parameters are calibrated by using homogenized micromechanical (HMM) solutions for the RVE for a few strain histories. The proposed model is validated by comparing the CDM results with HMM response of single and multiple fiber RVEs subjected to arbitrary loading history. Finally the HCDM model is incorporated in a macroscopic finite element code to conduct damage analysis in a structure. The effect of different microstructures on the macroscopic damage progression is examined through this study.

KEY WORDS: continuum damage mechanics, homogenization, interfacial debonding, cohesive zone element, principal damage coordinate system.

INTRODUCTION

C ONTINUUM DAMAGE MECHANICS (CDM) models provide a constitutive framework for reflecting damage induced stiffness reduction with the

introduction of effective damage parameters that represent overall material degradation (Chaboche, 1981; Kachanov, 1987; Lemaitre and Chaboche, 1990; Krajicinovic, 1996; Nemat-Nasser and Hori, 1999; Voyiadjis and Kattan, 2006). Damage and failure of composite materials is inherently a multiple scale phenomenon coupling different scales of damage initiation and progression. Two types of CDM models, namely phenomenological and micromechanical models, have been proposed in the literature for modeling failure of composite materials. The phenomenological CDM models (Chaboche, 1981; Ortiz, 1985; Simo and Ju, 1987; Chow and Wang, 1987; Matzenmiller et al., 1995; Chan et al., 2005) employ scalar, second order, and fourth order damage tensors using mathematically and thermodynamically consistent formulations of damage mechanics. Damage parameters are identified through macroscopic experiments and in general, they do not explicitly account for damage mechanisms in the microstructure. In Desmorat et al. (2007), a generalized damage law has been developed in terms of cumulative measure of internal sliding for monotonic, hysteretic, dynamic, and fatigue loadings without explicit consideration of micromechanics. The micromechanics-based approaches (Lene and Leguillon, 1982; Costanzo et al., 1995; Chaboche et al., 1998; Wriggers et al., 1998; Fish et al., 1999; Choi and Tamma, 2001; Ladeveze, 2002; Sharma et al., 2005; Ju et al., 2006), on the other hand conduct micromechanical analysis of a representative volume element (RVE) with subsequent homogenization, to predict evolving material damage behavior. The model by Ladeveze (2002) connects micromechanics with continuum for developing an anisotropic damage model with crack closure effects. Three homogenized parameters represent damage in the cracked ply and their dependence on stacking sequence is determined through 2D plane stress micromechanical simulations. Different damage mechanisms such as transverse microcracking, delamination, and fiber–matrix debonding are considered in this model. Various models in Allix and Hild (2002) also discuss similar development of the CDM models. With the exception of a few e.g., (Voyiadjis and Kattan, 1992; Fish et al., 1999; Kouznetsova et al., 2001; Raghavan and Ghosh, 2005; Voyiadjis et al., 2007), most damage models do not account for the evolution of damage or the effect of loading history. Significant error can consequently accrue in the solution of problems, especially those that involve nonproportional loading. Some of these homogenization studies have overcome this shortcoming through the introduction of simultaneous RVE-based microscopic and macroscopic analysis in each load step (Fish et al., 1999; Feyel and Chaboche, 2000; Massart et al., 2007). However, such approaches can be computationally very expensive since detailed micromechanical analyses need to be conducted in each load step at every integration point in elements of the macroscopic structure.

To overcome the shortcomings of macro–micro modeling of composites for predicting damage, Ghosh and coworkers (Raghavan and Ghosh, 2005; Ghosh et al., 2007) have developed a computationally efficient, anisotropic homogenization-based continuum damage mechanics (HCDM) model for composites undergoing microstructural damage. Specifically fiber–matrix interface debonding has been taken as the microstructural damage mechanism in these two dimensional analyses, for which micromechanical analyses are conducted by the Voronoi cell FEM model (Ghosh et al., 2000; Li and Ghosh, 2004).This model is constructed by homogenizing evolving damage variables in micromechanical analyses of a representative microstructural volume element of the composite. The homogenization-based continuum damage model (HCDM) has been successfully used for macroscopic analysis in multi-scale modeling of composites undergoing fiber–matrix interfacial debonding in Ghosh et al. (2007). In a multi-scale modeling framework, the use of a continuum damage mechanics model in regions of noncritical diffused damage evolution makes the overall computing extremely efficient. This model can avoid the need to perform micromechanical analysis at each load increment. However, it is necessary to zoom into the microstructure and perform pure microscopic analysis in critical regions of dominant crack propagation or localized instability to accurately predict catastrophic failure (Raghavan and Ghosh, 2004; Ghosh et al., 2001, 2007).

The 2D HCDM model in Raghavan and Ghosh (2005) does not incorporate the effects of the path dependent load history on the damage variables. Hence, its predictions are not accurate for e.g., nonproportional loading cases. The present paper develops a 3D HCDM model that can overcome these limitations through the introduction of a principal damage coordinate system (PDCS), which evolves with the load history. Such a coordinate system has been used in Chow et al. (2001) to predict formability of viscoplastic materials. The 3D HCDM model introduces functional forms of a fourth order damage tensor in terms of macroscopic strain components that are calibrated by micromechanical RVE analysis along different strain loading paths. Anisotropy and its evolution are also effectively treated in this model. Parametric representation of various damage tensors significantly enhances computational efficiency by avoiding the cumbersome strain space interpolations in Raghavan and Ghosh (2005). The HCDM model can be conveniently incorporated in any finite element code for efficient modeling of damage evolution in composite structures due to degrading microstructures.

The CDM model proposed has two main attributes. It has a very strong connection with the micromechanical phenomena. For example, one can relate the macroscopic damage energy to the amount of debonding or fiber cracking in the microstructure for any composite architecture. Thus, it can be used as an effective tool for microstructure design. The second is, through

the development of the CDM model, one can avoid tedious micro–macro computations, while getting the same accuracy and dependence on the microstructure and micromechanics. Hence, it can be coupled and used in any commercial software for major structural analyses.

This paper starts with a brief review of anisotropic continuum damage mechanics models of (Raghavan and Ghosh, 2005) in 'Anisotropic Continuum Damage Mechanics Model' section. 'Micromechanical RVE Model and Homogenization' section describes the micromechanical model with interfacial debonding followed by its homogenization. An orthotropic homogenization-based CDM or HCDM model is developed in the principal damage coordinated system (PDCS) is discussed in 'Evolution Equations for the Homogenization-based CDM Model' section. This section also discusses parameter calibration. 'Implementation of the HCDM Model in a Macroscopic Analysis Module' section provides the stress update procedure with HCDM in its implementation in a macroscopic finite element code for structural analysis. Validation of the HCDM model and a demonstrative structural application are presented in sections 'Numerical Examples for Validating the HCDM Model' and 'Macro–Micro Analysis of a Composite Structure with the HCDM Model' respectively. The effect of different microstructures on the structural damage growth is examined in these analyses.

ANISOTROPIC CONTINUUM DAMAGE MECHANICS MODEL

The general form of CDM models (see e.g., Kachanov, 1987), introduces a fictitious stress $\tilde{\Sigma}_{ij}$ acting on an effective resisting area ($\tilde{A}$). This is caused by reduction of the original resisting area A due to material degradation due to the presence of micro-cracks and stress concentration in the vicinity of cracks. In Simo and Ju (1987) and Raghavan and Ghosh (2005), the effective stress $\tilde{\Sigma}_{ij}$ is related to the actual Cauchy stress Σ_{ij} through a fourth order damage effect tensor M_{ijkl} as

$$\tilde{\Sigma}_{ij} = M_{ijkl}(\mathbf{D})\Sigma_{kl} \tag{1}$$

where M_{ijkl} is a function of a damage tensor $\mathbf{D} (= D_{ijkl}\mathbf{e_i} \otimes \mathbf{e_j} \otimes \mathbf{e_k} \otimes \mathbf{e_l})$. $\mathbf{D}$ can be a zero-th, second, or fourth order tensor, depending on the model employed. The hypothesis of equivalent elastic energy (Cordebois and Sidoroff, 1982; Chow and Wang, 1987) is used to evaluate M_{ijkl} and establish a relation between the damaged and undamaged stiffnesses. As discussed in Voyiadjis and Kattan (1992, 2006), this hypothesis specifically assumes that the elastic complimentary energy W_C in a damaged material with the actual

stress is equal to that in a hypothetical undamaged material with a fictitious effective stress, i.e.,

$$W_C(\mathbf{\Sigma}, \mathbf{D}) = \frac{1}{2}(E_{ijkl}(\mathbf{D}))^{-1}\Sigma_{ij}\Sigma_{kl} = W_C(\tilde{\Sigma}, \mathbf{0}) = \frac{1}{2}(E^o_{ijkl})^{-1}\tilde{\Sigma}_{ij}\tilde{\Sigma}_{kl} \qquad (2)$$

where $\mathbf{\Sigma} = \Sigma_{ij}\mathbf{e_i} \otimes \mathbf{e_j}$, E^o_{ijkl} is the elastic stiffness tensor in the undamaged state and $E_{ijkl}(\mathbf{D})$ is the stiffness in a damaged state. From Equations (1) and (2), the relation between the damaged and undamaged stiffnesses is established as

$$E_{ijkl} = (M_{pqij})^{-1}E^o_{pqrs}(M_{rskl})^{-T} \qquad (3)$$

where the exponent $-T$ corresponds to the transpose of the inverse of the fourth order $\mathbf{M}$ tensor. With the choice of an appropriate order of the damage tensor and the assumption of a function for M_{ijkl}, Equation (3) can be used to formulate a damage evolution model using micromechanics and homogenization. The anisotropic CDM model involving fourth order damage tensor, proposed in Raghavan and Ghosh (2005), introduces a damage evolution surface to delineate the interface between damaged and undamaged domains in the strain space (e_{ij}) as

$$F = \frac{1}{2}P_{ijkl}e_{ij}e_{kl} - \kappa(\alpha W_{\mathrm{d}}) = 0 \qquad (4)$$

where W_{d} is the dissipation of the strain energy density due to stiffness degradation that is expressed as (Carol et al., 1994):

$$W_{\mathrm{d}} = \int \frac{1}{2}e_{ij}e_{kl}\mathrm{d}E_{ijkl} \qquad (5)$$

Assuming associativity rule in the stiffness space, the evolution of the fourth order secant stiffness is obtained as

$$\dot{E}_{ijkl} = \dot{\lambda}\frac{\partial F}{\partial(\frac{1}{2}e_{ij}e_{kl})} = \dot{\lambda}P_{ijkl} \qquad (6)$$

P_{ijkl} is a fourth order symmetric negative definite tensor that corresponds to the direction of the rate of stiffness degradation tensor $\dot{E}_{ijkl}$, α is a scaling parameter and $\kappa(\alpha W_{\mathrm{d}})$ is a damage state variable. Calibration of the CDM model requires evaluation of κ, α, and P_{ijkl} in Equation (4). Calibration is done by comparison of the CDM model results with those from

homogenization of micromechanical RVE analysis, subject to different loads. Based on this comparison, P_{ijkl} is found to vary as a function of the strain e_{ij}, α is a constant and κ is a function of W_{d}. Details of the calibration process are discussed in 'Evolution Equations for the Homogenization-based CDM Model' section.

The CDM Model in Principal Damage Coordinate System

For a second order damage tensor D_{ij}, the damage effect tensor M_{ijkl} in Equation (1) has been formulated in Murakami (1988) as:

$$M_{ijkl} = (\delta_{ik} - D_{ik})^{-1}\delta_{jl} \tag{7}$$

D_{ij} is symmetric and it can describe the damage states which have at least orthotropic symmetry. For any arbitrary D_{ij} the corresponding effective stress tensor, obtained by substituting Equation (7) in Equation (1), may be unsymmetric. An implicit method of rendering the stress tensor symmetric has been suggested in Voyiadjis and Kattan (1996), which corresponds to a representation of the stress tensor in a fixed global coordinate system as

$$\Sigma_{ij} = \frac{\tilde{\Sigma}_{ik}(\delta_{kj} - D_{kj})^{-1} + (\delta_{il} - D_{il})^{-1}\tilde{\Sigma}_{lj}}{2} \tag{8}$$

The corresponding inverse of the damage effect tensor $[\mathbf{M}(D_{ij})]^{-1}$ is represented in a matrix form as:

$[\mathbf{M}(D_{ij})]^{-1} =$

$$\begin{bmatrix} 1-D_{11} & 0 & 0 & 0 & -D_{13} & -D_{12} \\ 0 & 1-D_{22} & 0 & -D_{23} & 0 & -D_{12} \\ 0 & 0 & 1-D_{33} & -D_{23} & -D_{13} & 0 \\ 0 & -\frac{1}{2}D_{23} & -\frac{1}{2}D_{23} & 1-\frac{1}{2}(D_{22}+D_{33}) & -D_{12} & -D_{13} \\ -\frac{1}{2}D_{13} & 0 & -\frac{1}{2}D_{13} & -\frac{1}{2}D_{12} & 1-\frac{1}{2}(D_{11}+D_{33}) & -D_{23} \\ -\frac{1}{2}D_{12} & -\frac{1}{2}D_{12} & 0 & -\frac{1}{2}D_{13} & -\frac{1}{2}D_{23} & 1-\frac{1}{2}(D_{11}+D_{22}) \end{bmatrix} \tag{9}$$

This can be substituted in Equation (3) to update the damaged stiffness E_{ijkl} from the initial undamaged stiffness E_{ijkl}^{o}.

Numerical examples by the authors in Raghavan and Ghosh (2005) have shown that material symmetry is considerably affected by damage evolution

in composite microstructures. Different load paths will yield different damage evolution profiles in the microstructure. This will result in different changes of the material symmetry in E_{ijkl}. For example, in a fixed coordinate system, an RVE exhibiting orthotropy in E^o_{ijkl} can exhibit general anisotropy with evolving damage under multi-axial loading. The anisotropic E_{ijkl} will couple normal and shear strain components in the elastic energy expression in the fixed coordinate system. However, when the strains are represented in a coordinate system that corresponds to the principal damage axes, the coupling terms in the stiffness E_{ijkl} reduce to near vanishing values and the initial symmetry properties are retained.

The present work assumes orthotropy of the homogenized stiffness matrix in the PDCS. The damage effect tensor M_{ijkl} corresponding to Equation (9) has a diagonal representation in this coordinate system and consequently, the initial material symmetry is retained throughout the damage evolution process. Determination of the continuously evolving PDCS requires the determination of the second order damage tensor D_{ij} and subsequent evaluation of its eigenvectors at each step of the incremental loading process. For known values of E^o_{ijkl} and E_{ijkl}, substitution of Equation (9) in Equation (3) results in a system of nonlinear algebraic equations in D_{ij}. Since there are nine independent components of the orthotropic stiffness tensor E_{ijkl} and six independent components of the symmetric D_{ij}, a nonlinear least squares minimization solver is used to solve for D_{ij}. Subsequently, the eigenvectors of D_{ij}, namely $\mathbf{e}_{\mathbf{D}1}, \mathbf{e}_{\mathbf{D}2}$, and $\mathbf{e}_{\mathbf{D}3}$ are evaluated and the transformation matrix $[\mathbf{Q}]^D = [\mathbf{e}_{\mathbf{D}1} \ \mathbf{e}_{\mathbf{D}2} \ \mathbf{e}_{\mathbf{D}3}]$ is formed. The rotation matrix $[\mathbf{Q}]^D$ transforms the global coordinate system to the PDCS.

Evolution of PDCS for Different Load Histories

To examine the evolution of PDCS with different load histories, a micromechanical analysis problem of a simple unit cell RVE is conducted. The elastic RVE consists of a circular fiber of 20% volume fraction in a square matrix as shown in Figure 1. To allow debonding, the fiber–matrix interface is modeled using cohesive zone elements as discussed in 'Micromechanical RVE Model and Homogenization' section. Micromechanical analysis is followed by homogenization to evaluate evolving stiffnesses in the composite. Two load histories are considered for the analyses.

1. *Case a:* Proportional loading with strain path $(e_{12}/e_{11}) = \mathrm{constant} \, (\neq 0)$ and $e_{22} = 0$.
2. *Case b:* Nonproportional loading with two loading segments: (i) strain path of $e_{11} \neq 0, e_{22} = e_{12} = 0$ in the first half of the loading; (ii) strain path of $(e_{12}/e_{11}) = \mathrm{constant} \, (\neq 0), e_{22} = 0$ in the second half.
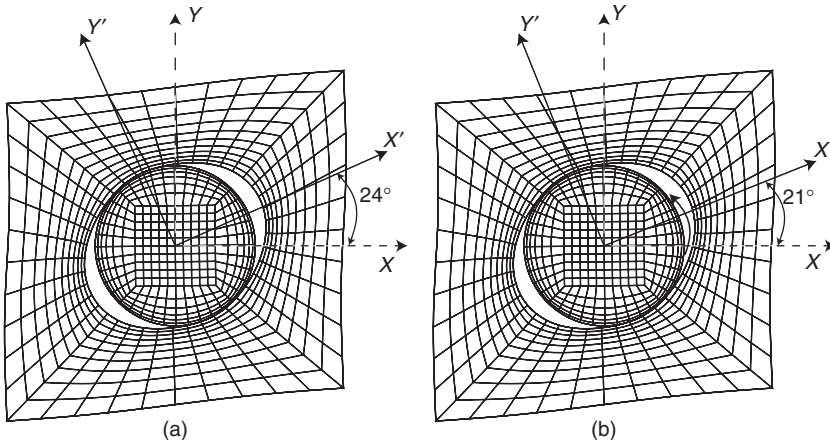
Figure 1. *Rotation of the PDCS for (a) proportional and (b) nonproportional load histories.*

The final state of the macroscopic strain e_{ij} is identical for both the cases. Along each of these load paths, the homogenized secant stiffness of the damaging material E_{ijkl} is calculated, followed by determination of the PDCS. Figure 1(a) and (b) show the orientation of the PDCS in the final deformed configuration for the two cases. For the proportional loading case (a), the orientation of the damage axes jumps to and remains fixed at $24°$ with respect to the global axes throughout damaging process. For the nonproportional loading case (b), the PDCS coincides with the global coordinate system in simple tension during the first half of loading. In the last half of the loading, the PDCS continuously rotates to a final position of $21°$ orientation. Certainly in this case, the PDCS rotation should be incorporated in the homogenization-based continuum damage mechanics or HCDM model to account for the damage history.

MICROMECHANICAL RVE MODEL AND HOMOGENIZATION

Micromechanical analyses of identified RVEs of the composite microstructure are necessary ingredients for the development of a homogenization-based continuum damage mechanics or HCDM model. Important aspects of a 3D micromechanical model are discussed next.

Cohesive Zone Model for Interfacial Debonding

A 3D micromechanical model for composite microstructures undergoing fiber–matrix interfacial debonding has been developed in Swaminathan

et al. (2006b). In this model, the fiber–matrix interface behavior in the normal and tangential directions is described by a nonlinear 3D cohesive zone model with bilinear traction–displacement relations. Bilinear cohesive zone models have yielded satisfactory agreement with experiments for composites described in Chandra et al. (2002) and Li and Ghosh (2004). The interface is represented by a set of cohesive springs of infinitesimal length that are attached to the fiber and the matrix at opposite ends. With increasing displacement the traction across the interface reaches a maximum value, then decreases with further displacement increase, and finally vanishes indicating failure of the spring. Needleman (1990, 1992) has proposed cohesive zone models with polynomial and exponential functions for the traction–displacement jump relation. Ortiz and co-workers (Camacho and Ortiz, 1996; Ortiz and Pandol, 1999) have developed irreversible cohesive laws for the unloading path after the interfacial softening.

In the cohesive zone model used in this work, the relation between traction $T(= \sqrt{T_n^2 + T_{t1}^2 + T_{t2}^2})$ and the effective opening displacement $\delta(= \|\mathbf{u_m} - \mathbf{u_f}\|)$ is given in terms of a free energy potential as

$$T = \sqrt{T_n^2 + T_{t1}^2 + T_{t2}^2} = \frac{\partial \phi(\delta_n, \delta_{t1}, \delta_{t2}, q)}{\partial \delta} \tag{10}$$

where (T_n, T_{t1}, T_{t2}) are normal and tangential components of the interfacial traction and q are internal variables that account for the inelastic process of decohesion. The effective opening displacement jump, δ, in 3D is defined as

$$\delta = \sqrt{\delta_n^2 + \beta^2 \delta_t^2} \tag{11}$$

Here, δ_n is the displacement jump in normal direction, $\delta_t(= \sqrt{\delta_{t1}^2 + \delta_{t2}^2})$ is the net displacement jump in tangential direction across the interface. β is a factor that controls the contribution of the tangential component to the effective displacement jump. The scalar form of the $T - \delta$ relation in the bilinear model is obtained from equation (9) as

$$T = \begin{cases} \dfrac{\sigma_{\max}}{\delta_c} \delta & \text{if } \delta \leq \delta_c \quad \text{(hardening region)} \\[2mm] \dfrac{\sigma_{\max}}{\delta_c - \delta_e}(\delta - \delta_e) & \text{if } \delta_c < \delta \leq \delta_e \quad \text{(softening region)} \\[2mm] 0 & \text{if } \delta > \delta_e \quad \text{(complete debonding)} \end{cases} \tag{12}$$

Consequently, the normal and tangential tractions are derived from the relations:

$$
T_n = \frac{\partial \phi}{\partial \delta_n}
\begin{cases}
\dfrac{\sigma_{\max}}{\delta_c} \delta_n & \text{if } \delta \leq \delta_c \\[2ex]
\dfrac{\sigma_{\max}}{\delta} \dfrac{\delta - \delta_e}{\delta_c - \delta_e} \delta_n & \text{if } \delta_c < \delta \leq \delta_e \ (i = 1, 2) \\[2ex]
0 & \text{if } \delta > \delta_e
\end{cases}
\tag{13}
$$

and

$$
T_{ti} = \frac{\partial \phi}{\partial \delta_{ti}}
\begin{cases}
\dfrac{\sigma_{\max}}{\delta_c} \beta^2 \delta_{ti} & \text{if } \delta \leq \delta_c \\[2ex]
\dfrac{\sigma_{\max}}{\delta} \dfrac{\delta - \delta_e}{\delta_c - \delta_e} \beta^2 \delta_{ti} & \text{if } \delta_c < \delta \leq \delta_e \quad (i = 1, 2) \\[2ex]
0 & \text{if } \delta > \delta_e
\end{cases}
\tag{14}
$$

For a positive normal displacement δ_n, the traction at the interface increases linearly to a maximum value of max $\sigma_{\max}$ corresponding to δ_c. After that, the traction starts decreasing with increasing separation and finally reaches zero at a value of δ_e. The unloading behavior in the hardening region follows the same slope as that of the loading path. In the softening region, unloading is assumed to follow a different linear path back from the current position to the origin with a reduced stiffness. This is expressed as

$$
T = \frac{\sigma_{\max}}{\delta_{\max}} \frac{\delta_{\max} - \delta_e}{\delta_c - \delta_e} \delta \qquad \delta_c < \delta_{\max} < \delta_e \text{ and } \delta < \delta_{\max}
\tag{15}
$$

Reloading follows the unloading slope till it meets the point of unloading in the softening plot, and then continues along the softening plot. This demonstrates the irreversible nature of the damage process. The normal component of the traction is transferred through the normal springs, while the shear component of the traction is transferred through the tangential springs. Both the normal and the tangential tractions vanish when interface debonds completely i.e., $\delta \geq \delta_e$. Also, the magnitudes of the tangential traction–displacement relation are independent of the sign, and hence the behavior is the same for both positive and negative tangential separations δ_{i1} and δ_{i2}. If the normal displacement is negative, i.e., during compression, stiff penalty springs with high stiffness are introduced between the node-pairs at the interface to prevent penetration.

Implementation of the Cohesive Zone Model in the RVE Model

The 3D interface elements using the cohesive laws are developed in the user defined element (UEL) subroutine of the commercial FE code ABAQUS (Abaqus, 2001). As detailed in Swaminathan et al. (2006b), the interface elements are made up of two eight-noded quadrilateral surfaces that are compatible with the standard 20-node brick elements. The corresponding cohesive interface elements have 16 nodes with a quadratic displacement interpolation, which leads to a total of 48 degrees of freedom per element. Integration in each element is conducted by Gaussian quadrature using nine integration points. The cohesive interface elements are compatible with the 20-noded quadratic brick elements that are used to model the fiber and matrix phases. A typical RVE model developed for analysis in ABAQUS is shown in Figure 2(a). In the initial unloaded state, the interface nodes on the matrix and fiber surfaces share the same coordinates. With the application of an external loads and displacements, the interface surfaces move and separate from one another, as the adjacent solid elements deform. The relative normal and tangential tractions for the interface elements are calculated at the element integration points according to the traction separation laws Equation (10)–(14) in the cohesive zone model. Details of the implementation procedure has been discussed in Swaminathan et al. (2006b).

Homogenization and Stiffness Evaluation

Components of the homogenized elastic stiffness tensor E_{ijkl}, are calculated by solving six independent micromechanical boundary value problems of the RVE. The RVE is each case is subjected to periodicity displacement conditions on the boundary. These conditions are enforced by constraining nodes on opposite faces of the RVE boundary to deform in a periodic manner. A given macroscopic or average strain e_{ij} is applied on the RVE by decomposing the displacement on the boundary into a macroscopic averaged and a periodic part as discussed in Pellegrino et al. (1999) and Segurado and Llorca (2002), i.e.,

$$u_i = e_{ij}x_j + \tilde{u}_i \qquad (16)$$

Since the periodic part $\tilde{u}_i$ is equal on corresponding nodes of opposite faces of the RVE (say n_1^p and n_2^p), the total displacement at these nodes are related as

$$(u_i)_{n_2^p} - (u_i)_{n_1^p} = e_{ij}\Delta x_j \qquad (17)$$
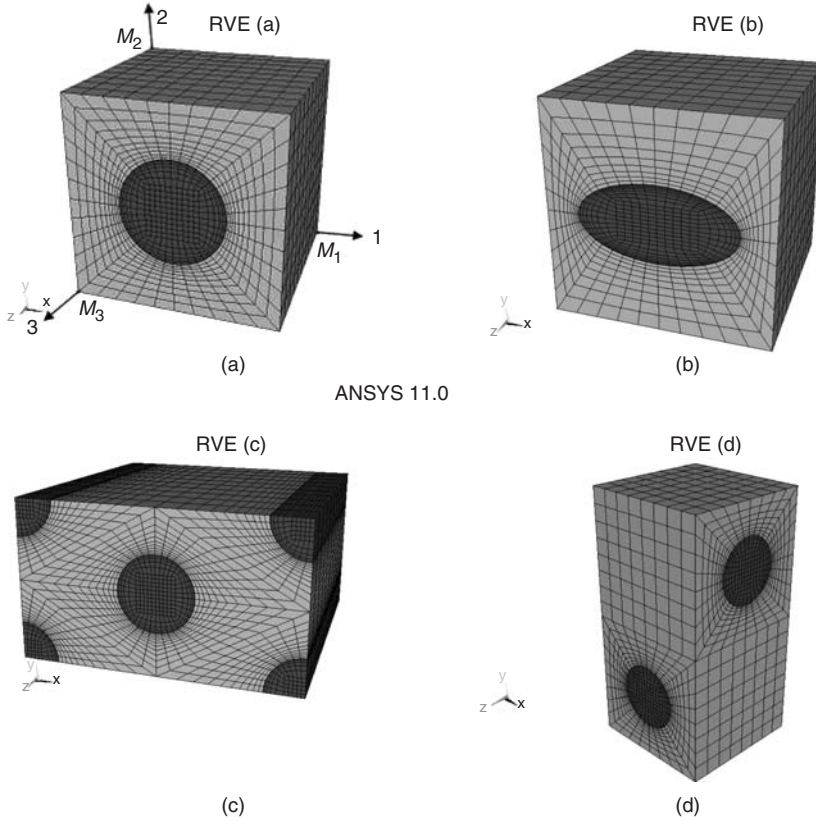
Figure 2. *Finite element mesh for (a) RVE with a cylindrical fiber, (b) RVE with an elliptical fiber, (c) RVE with hexagonal arrangement of fibers, and (d) RVE with two perpendicular fibers.*

where Δx_i are the relative coordinates of nodes on opposite faces. Macroscopic strains are then applied, in conjunction with the periodicity constraints, by fixing a corner node and specifying the displacement on master nodes $M_1, M_2,$ and M_3 that belong to orthogonal faces as shown in Figure 2(a).

For evaluating the homogenized elastic stiffness tensor E_{ijkl}, periodic boundary value problems of the RVE are solved by applying only a single unit strain component. These correspond to six boundary value problems: *Case 1: $e_{11} = 1.00$,* all other components = 0.0, *Case 2: $e_{22} = 1.00$,* all other components = 0.0, *Case 3: $e_{12} = 1.00$,* all other components = 0.0, etc. Finally, the homogenized or macroscopic stresses Σ_{ij} are obtained by volume averaging as

$$\Sigma_{ij} = \frac{1}{Y} \int_Y \sigma_{ij}(Y) \mathrm{d}Y \qquad (18)$$

In addition the homogenized strains, required for calibrating the HCDM model, are evaluated by volume averaging the micromechanical solutions as

$$e_{ij} = \frac{1}{Y}\int_Y \epsilon_{ij}(Y)\mathrm{d}Y + \frac{1}{2Y}\int_{\partial Y_{\mathrm{int}}} ([u_i]n_j + [u_j]n_i)\mathrm{d}S \qquad (19)$$

Here, σ_{ij} and ϵ_{ij} are RVE-based microscopic stresses and strains, respectively and Y is the RVE domain. Y_{int} corresponds to the fiber–matrix interface domain and $[u_i]$ denotes the jump in displacement components across the interface with outward normal n_i.

EVOLUTION EQUATIONS FOR THE HOMOGENIZATION-BASED CDM MODEL

The damage evolution surface of Equation (4) is rewritten in the PDCS as

$$F' = \frac{1}{2}e'_{ij}P'_{ijkl}e'_{kl} - \kappa'(W_{\mathrm{d}}) = 0 \qquad (20)$$

where the prime in the superscript denotes quantities expressed in the PDCS using the transformation laws

$$E'_{ijkl} = Q_{ip}Q_{jq}Q_{kr}Q_{ls}E_{pqrs} \text{ and } e'_{ij} = Q_{ik}Q_{jl}e_{kl} \qquad (21)$$

and Q_{ij} is the transformation matrix. The corresponding rate of stiffness degradation in PDCS is

$$\dot{E}'_{ijkl} = \dot{\lambda}\frac{\partial F'}{\partial(\frac{1}{2}e'_{ij}e'_{kl})} = \dot{\lambda}P'_{ijkl} \qquad (22)$$

Parametric Forms and Parameter Calibration

DAMAGE STATE VARIABLE κ'

The damage function $\kappa'(\alpha W_{\mathrm{d}})$ is evaluated for a reference loading path, and results for all other strain paths are scaled with respect to this reference value. For the reference loading path ($e'_{11} \neq 0$, all other $e'_{ij} = 0$), setting $P'_{1111} = 1$, κ' is determined from damage surface of Equation (20) as

$$\kappa' = \frac{1}{2}(e'_{11})^2 \qquad (23)$$

The function $\kappa'(W_d)$ is determined from the micromechanical analysis by evaluating W_d at each strain increment. The $\kappa' - W_d$ plots for four different strain paths are shown with circular marks in Figure 3. The loading cases are:

(*Case 1*:) Simple shear: $e_{12} = 0.012$

(*Case 2*:) Tension–torsion: $e_{11} = 0.006, e_{12} = 0.010$

(*Case 3*:) Multi-axial tension–torsion: $e_{11} = 0.009, e_{22} = 0.002, e_{12} = 0.006$

(*Case 4*:) Uniaxial tension: $e_{11} = 0.012$

W_d remains zero in these plots, till κ' exceeds a threshold value corresponding to the initiation of debonding induced microscopic damage. Subsequently, W_d increases rapidly, signaling substantial material deterioration during the initial stages of damage. Eventually, W_d saturates at a value W_d^F corresponding to configuration with arrested debond or fully debonded interface. Very little material degradation due to damage occurs beyond this saturation value. The behavior of the plots are similar; however, the value of W_d^F differs for the different strain histories. The variability of the saturation damage energy W_d^F with different loading paths in the 3D strain space can be taken into account using the scaling factor $\alpha(e_{ij})$ in Equation (4). However, such an approach requires evaluation and storage of $\alpha(e_{ij})$ for a large number of individual loading paths for interpolation.
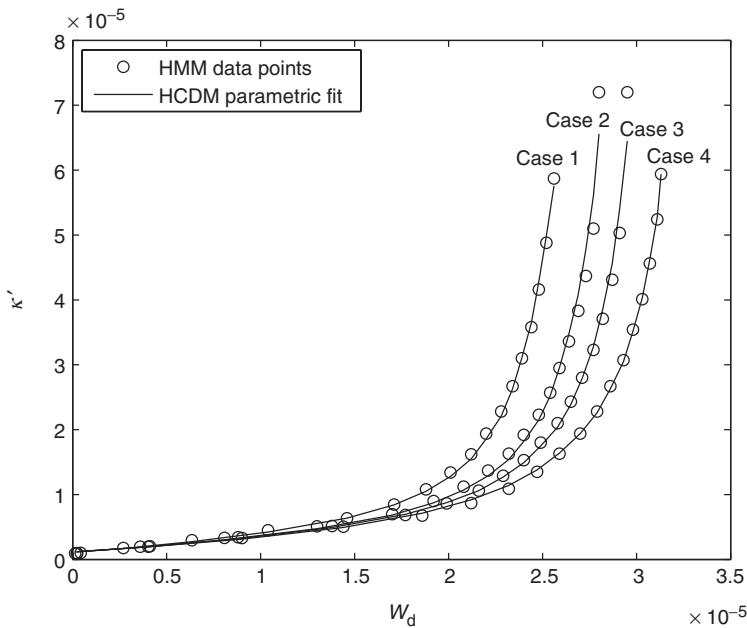
Figure 3. *Functional representation of the* $\kappa' - W_d$ *relation from homogenized micromechanics (HMM) data points.*

To avoid this approach in the 3D analysis, novel functional forms of κ' are introduced to explicitly describe its dependence on the macroscopic strain components e_{ij}, as well as on W_d. Three invariant forms of the strain components, consistent with anisotropic material properties model are used in these functions. They are:

$$I_1 = \frac{1}{3}(Ae_{11} + Be_{22} + Ce_{33})$$

$$J_2 = F\left(e_{22}^d - e_{33}^d\right)^2 + G\left(e_{33}^d - e_{11}^d\right)^2 + H\left(e_{11}^d - e_{22}^d\right)^2 + L\left(e_{12}^d\right)^2 + M\left(e_{13}^d\right)^2 + N\left(e_{23}^d\right)^2$$

$$J_3 = O\left(e_{11}^d e_{22}^d e_{33}^d\right) + P\left(e_{11}^d (e_{23}^d)^2\right) + Q\left((e_{12}^d)^2 e_{33}^d\right)$$

$$+ R\left(e_{13}^d e_{12}^d e_{23}^d\right) + S\left((e_{13}^d)^2 e_{22}^d\right) \tag{24}$$

where $e_{ij}^d = e_{ij} - \frac{1}{3}\delta_{ij}e_{kk}$ is the deviatoric strain tensor. The invariants I_1, J_2, and J_3 are respectively linear, quadratic, and cubic functions of e_{ij}. The constants $A, B, C, F, G, \ldots, S$ are introduced to characterize the state of anisotropy in the damaged material. The function J_2 is similar to that used in the anisotropic yield criterion for elasto-plasticity proposed by Hill (1948). The functional form of κ' is developed to conform to the plots of Figure 3, and is expressed as:

$$\kappa'(I_1, J_2, J_3, W_d) = b_0 + f(I_1, J_2, J_3)[1 + b_1\tan(b_2 W_d)] \tag{25}$$

The form decomposes its dependence on the dissipation energy and the strain. The latter dependence is represented by a polynomial function of the invariants as:

$$f(I_1, J_2, J_3) = a_0 + a_1 I_1 + a_2 J_2 + a_3 J_3 + a_4 I_1^2 + a_5 I_1 J_2 + \ldots \tag{26}$$

The constants $A, B, C, \ldots$ in Equation (24), b_0, b_1, b_2 in Equation (25), and $a_0, a_1, \ldots$ in Equation (26) are determined by a nonlinear least squares minimization of the difference between results of micromechanical analysis and those from the functional form in Equation (25), i.e.,

$$\text{minimize} \sum_{i=1}^{N_{\text{ref}}} \left[\kappa'_{\text{ref}} - \kappa'(I_1, J_2, J_3, W_d)\right]_i^2 \tag{27}$$

Micromechanical analysis of the RVE is conducted for N_{ref} different strain histories to explicitly compute the values of κ'_{ref}. A fifth order polynomial

function in Equation (26) yields good convergence properties for the least square residual. Figure 3 satisfactorily compares the $\kappa' - W_d$ plots by the function in Equation (25) with results from the micromechanical analysis for the different strain paths.

DAMAGE SURFACE PARAMETER P'_{ijkl}

In the incremental finite element formulation for evolving damage, the backward Euler method is used to integrate the rate of stiffness degradation in Equation (22). Corresponding to the strain increment from step n to step $n + 1$, the parameter P'_{ijkl} may be expressed as

$$(P'_{ijkl})_{n+1} = \frac{(E'_{ijkl})_{n+1} - (E'_{ijkl})_n}{\lambda_{n+1} - \lambda_n} \tag{28}$$

where $(E'_{ijkl})_{n+1}$ is the secant stiffness at the end of the increment. As explained in 'Cohesive Zone Model for Interfacial Debonding' section, the secant stiffness is calculated by unloading to the origin from the current state of stress. Substituting this into the damage evolution Equation (20) at the end of the increment yields the incremented form of the damage surface as

$$\frac{1}{2}(e'_{ij})_{n+1}\left(\frac{(E'_{ijkl})_{n+1} - (E'_{ijkl})_n}{\lambda_{n+1} - \lambda_n}\right)(e'_{kl})_{n+1} - \kappa'_{n+1} = 0 \tag{29}$$

where $\kappa'_{n+1}(I_1, J_2, J_3, W_d)$ represents the size of the parametric damage surface and $(W_d)_{n+1}$ at the end of the interval is evaluated by using the backward Euler integration method. The parameter λ_{n+1} is then evaluated from the relation

$$\lambda_{n+1} = \lambda_n + \frac{\frac{1}{2}(e'_{ij})_{n+1}\left((E'_{ijkl})_{n+1} - (E'_{ijkl})_n\right)(e'_{kl})_{n+1}}{\kappa'_{n+1}} \tag{30}$$

$(P'_{ijkl})_{n+1}$ may be subsequently determined from Equation (28). The direction of the rate of stiffness degradation varies continuously with damage evolution with increasing loads. From Equation (22) this implies that P'_{ijkl} also varies accordingly. A polynomial function form is derived for the components P'_{ijkl} in terms of the anisotropic invariants of strain defined in Equation (24), as

$$P'_{ijkl}(I_1, J_2, J_3) = c_0^{ijkl} + c_1^{ijkl}I_1 + c_2^{ijkl}J_2 + c_3^{ijkl}J_3 + c_4^{ijkl}I_1^2 + c_5^{ijkl}I_1J_2 + \dots \tag{31}$$

Again, the coefficients c_p^{ijkl} in Equation (31) are determined by a nonlinear least square equation solver. In this method, the square of the difference in

P'_{ijkl} obtained from micromechanical analysis and the functional form for a few representative strain paths, is minimized, i.e.,

$$\text{minimize} \sum_{i=1}^{N_{\text{ref}}} \Big[(P'_{ijkl})_{\text{ref}} - P'_{ijkl}(I_1, J_2, J_3) \Big]_i^2 \tag{32}$$

The subscript 'ref' corresponds to data points obtained from micromechanical analysis. Figure 4 shows a comparison of the micromechanical results and the calibrated function in Equation (31) for an RVE under uniaxial tension. With a fifth order polynomial function (30), the root mean square error is observed to be $< 3\%$. The coefficients can be used subsequently, for computing P'_{ijkl} for any given strain e_{ij} during the macroscopic analysis.

IMPLEMENTATION OF THE HCDM MODEL
IN A MACROSCOPIC ANALYSIS MODULE

The HCDM model is implemented for macroscopic finite element analysis using the user material interface (UMAT) in the commercial
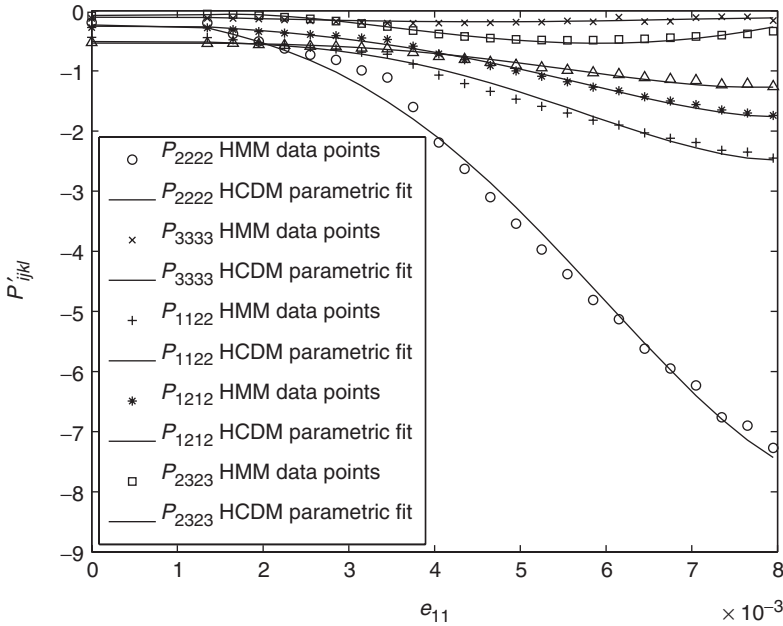
Figure 4. *Functional representation of $P'_{ijkl} - e_{11}$ relation for uniaxial tension from homogenized micromechanics (HMM) data points.*

code ABAQUS. In an incremental solution process, subscripts n and $n + 1$ correspond to values at the beginning and end of the n- th increment, respectively. At each integration point of an element in the FE model, the stresses $(\Sigma_{ij})_{n+1}$ are obtained from known values of the strain $(e_{ij})_{n+1}$ and state variables at n using the HCDM constitutive model. The essential steps in the UMAT update algorithm for the n- th increment are described subsequently.

1. Given $(e_{ij})_{n+1}$, evaluate $(I_1)_{n+1}, (J_2)_{n+1}$, and $(J_3)_{n+1}$ using Equation (24) and subsequently $(P'_{ijkl})_{n+1}$ using Equation (31).
2. Initialize variables at the start of each iteration algorithm for solving the damage evolution problem.

- Assume that the starting value of the PDCS rotation tensor $(Q_{ij})_{n+1}^0 = (Q_{ij})_n$.
- Evaluate the starting value of the damage surface function $(F'_{n+1})^0 = \frac{1}{2}(e'_{ij})_{n+1}(P'_{ijkl})_{n+1}(e'_{kl})_{n+1} - \kappa'_n$.
- If $(F'_{n+1})^0 \leq 0$ there is no additional damage. In this case, proceed to step 7 with unchanged secant stiffness tensor $(E_{ijkl})_{n+1} = (E_{ijkl})_n$.

3. For the I-th iteration, damage evolution takes place if: $\frac{1}{2}(e'_{ij})_{n+1}(P'_{ijkl})_{n+1}(e'_{kl})_{n+1} - \kappa'_n > 0$. In this case, determine:

- $(\kappa'_{n+1})^I = \frac{1}{2}(e'_{ij})_{n+1}((P'_{ijkl})_{n+1})^I(e'_{kl})_{n+1}$, and
- W_d by inverting the $\kappa' - W_d$ relation in Equation (25) as

$$((W_d)_{n+1})^I = \frac{1}{b_2}\tan^{-1}\left(\frac{1}{b_1}\left(\frac{(\kappa'_{n+1})^I - b_0}{(f_{n+1})^I(I_1, J_2, J_3)} - 1\right)\right) \tag{33}$$

4. Using the backward Euler method to integrate $\dot{W}_d$, determine

$$(\lambda_{n+1})^I = \lambda_n + \frac{2(((W_d)_{n+1})^I - (W_d)_n)}{(e'_{ij}P'_{ijkl}e'_{kl})_{n+1}^I} \tag{34}$$

5. Update the secant stiffness using the relation

$$(E'_{ijkl})_{n+1}^I = (E'_{ijkl})_n + (\lambda_{n+1}^I - \lambda_n)(P'_{ijkl})_{n+1}^I \tag{35}$$

6. Determine the PDCS rotation matrix $(Q_{ij})_{n+1}^I$ from the eigenvectors of $(D_{ij})_{n+1}^I$, corresponding to the updated secant stiffness $(E_{ijkl})_{n+1}^I$ using the

procedure described in section 'The CDM Model in Principal Damage Coordinate System'. If convergence in the rotation matrix is achieved, i.e.,

$$\text{If max } |((Q_{ij})_{n+1})^I - ((Q_{ij})_{n+1})^{I-1}| \leq TOL, \forall i,j = 1,2,3$$

then proceed to step 7. Otherwise, return to step 3 and continue iteration.
7. Update macroscopic stresses with the converged value of the secant stiffness matrix $(E_{ijkl})_{n+1}$ as

$$(\Sigma_{ij})_{n+1} = (E_{ijkl})^I_{n+1}(e_{kl})_{n+1} \tag{36}$$

NUMERICAL EXAMPLES FOR VALIDATING THE HCDM MODEL

The orthotropic 3D homogenization-based CDM (HCDM) model is validated by solving a few numerical examples. Results obtained from macroscopic simulations using the HCDM model are compared with homogenized micromechanical or HMM results for the RVE. The HMM model is obtained by homogenizing or volume averaging the micromechanical stresses and strains in the RVE subjected to periodic boundary conditions with imposed macroscopic strain as done in Ghosh et al. (2001) and Raghavan and Ghosh (2005). The macroscopic finite element model implementing the HCDM constitutive relations, consists of a single eight-noded quadrilateral element. Four 3D fiber–matrix composite RVEs with different morphological arrangements are considered for this validation study. These are:

- (a) Unidirectional 3D uniform composite microstructure with fibers arranged in a rectangular array. The RVE is a unit cell containing a single cylindrical fiber of volume fraction 20%. This is shown in Figure 2(a).
- (b) Unidirectional 3D uniform composite microstructure with fibers arranged in a rectangular array. The RVE is a unit cell containing a single fiber of elliptical cross-section as shown in Figure 2(b). Volume fraction is 20% and the aspect ratio of the elliptical cross-section is a/b = 2.
- (c) Unidirectional 3D composite microstructure with hexagonal arrangement of fibers. The RVE contains cylindrical fibers as shown in Figure 2(c), with a fiber volume fraction is 20%.
- (d) Cross-ply 3D composite microstructure with its RVE consisting of two cylindrical fibers oriented at 90° with respect to each other as shown in Figure 2(d). The fiber volume fraction in the RVE is 20%.

Material properties of the elastic matrix are $E_m = 4.6\,\text{GPa}$, $\nu_m = 0.4$, while for the elastic fiber they are $E_c = 210\,\text{GPa}$, $\nu_c = 0.3$. Cohesive zone parameters for the interface are $\delta_c = 5.0 \times 10^{-5}\,\text{m}$, $\delta_e = 20 \times 10^{-4}\,\text{m}$, and $\sigma_m = 0.02\,\text{GPa}$.

Micromechanical analyses of the RVEs are conducted by enforcing periodic displacement boundary conditions and imposing the macroscopic strain fields on the RVE. Both proportional and nonproportional macroscopic strain loading conditions are applied as follows:

1. **L1** Proportional uniaxial tension loading: $e_{11} \neq 0$, all other $e_{ij} = 0$ for the entire loading process. This is taken as the reference loading path.
2. **L2** Proportional, combined tension/shear loading: $e_{11} \neq 0, e_{22} \neq 0$, $e_{12} \neq 0$, all other $e_{ij} = 0$ for the entire loading process.
3. **L3** Nonproportional loading: $e_{11} \neq 0$, all other $e_{ij} = 0$ (uniaxial tension in the first half of the loading); and $e_{11} \neq 0, e_{12} \neq 0$, all other $e_{ij} = 0$ (combined tension/shear in the second half of the loading).

Contour plots of the microscopic stress in the different 3D RVEs, subjected to uniaxial tension in the x_1 direction are shown in Figures 5(a)–(d). The figures also show the extent of debonding for all the microstructures.
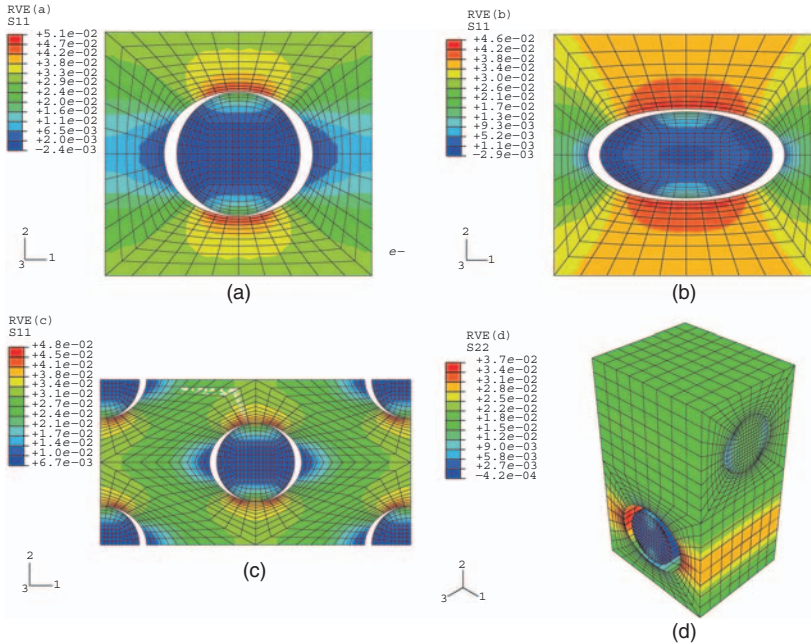

Figure 5. Microscopic stress contour plots in the RVEs (a), (b), (c), and (d), subjected to a uniaxial tensile strain $e_{11} = 0.004$.

The various parameters in the HCDM model are calibrated for the RVEs (a)–(d) following the procedure outlined in 'Evolution Equations for the Homogenization-based CDM Model' section. The constants $A, B, C, F, G, \ldots, S$ in Equation (24) for the strain invariants are evaluated for all four RVEs and reported in Table 1. The constants exhibits symmetry with respect to x_1 and x_2 directions for the RVE (a), and with respect to x_1 and x_3 directions for the RVE (d) with two perpendicular fibers. Since there are many calibrated constants in the expressions for κ' and P'_{ijkl}, only a few representative values are given for the RVE (a) with a single cylindrical fiber. These are: $b_0 = 0.1E - 6$; $b_1 = 12.44$; $b_2 = 0.44E5$; $a_0 = 0.42$; $a_1 = 3.08$; $a_2 = 2.44$; $a_3 = 74.2$. For P_{1111}, some of the constants are $c_0^{1111} = -1.16$; $c_1^{1111} = -0.144$; $c_2^{1111} = -0.615$; $c_3^{1111} = -0.144$. Figures 6(a)–(d) show plots of damage surface state variable κ as a function of W_d and the first strain invariant I_1 for the RVEs (a)–(d), respectively. The functions are generated using Equation (25). In all cases, κ' increases rapidly with W_d, which attains a maximum value as the damage in the RVE saturates. Although nature of the $\kappa' - W_d$ relation is similar for all cases, the sensitivity of κ to I_1 is seen to be significantly different for various RVEs.

Figures (7)–(10) compare the macroscopic stress–strain plots obtained from macroscopic analysis using HCDM with homogenized micromechanical or HMM results for the three load cases considered. The excellent match in most cases corroborates the satisfactory performance of the HCDM model. An important observation from these results is the sensitivity of the HCDM behavior to the microstructural architecture in response to

Table 1. Constants in the parametric representation of I_1, J_2, and J_3 in Equation (23) for various RVEs.

| Constants in Equation (23)	RVE in Figure 2(a)	RVE in Figure 2(b)	RVE in Figure 2(c)	RVE in Figure 2(d)
A	0.32	0.30	0.28	0.22
B	0.32	0.59	0.28	0.21
C	0.02	0.89	0.27	0.22
F	0.02	0.35	0.10	0.65
G	0.02	0.35	0.09	0.71
H	0.42	1.64	0.11	0.65
L	0.18	0.41	1.70	1.76
M	0.38	2.28	0.94	0.23
N	0.38	2.35	0.94	1.76
O	0.00	1.87	0.22	0.45
P	0.16	0.98	0.47	0.43
Q	0.34	0.05	0.24	0.43
R	0.13	0.41	0.26	0.07
S	0.16	0.13	0.47	0.12
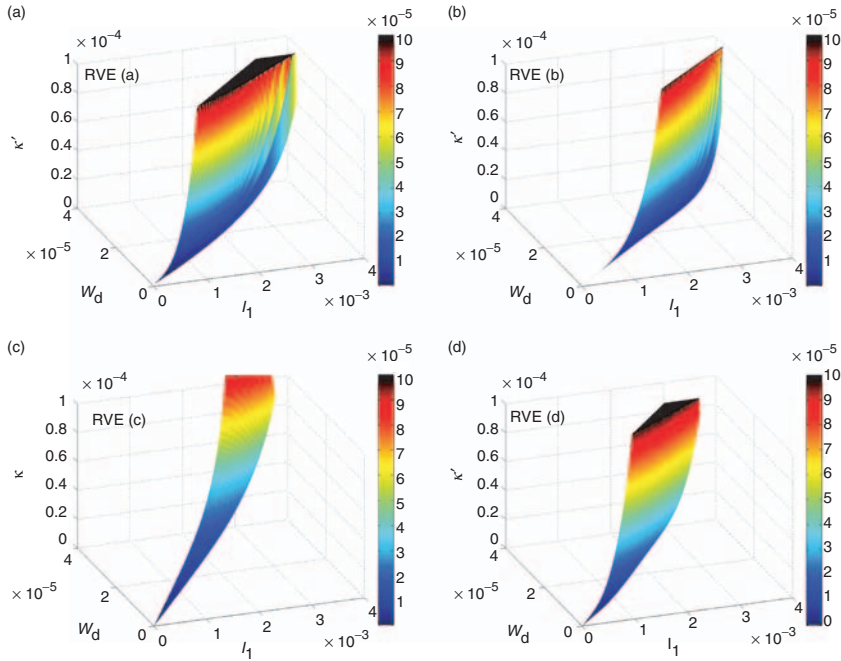
Figure 6. $\kappa \prime - W_d$ plot as a function of I_1 for RVEs (a), (b), (c), and (d).

different loads. The RVE (a) subjected to loading (L1) shows rapid material degradation with increasing strain as the interface undergoes debonding in Figure 7(a). The stiffness stabilizes at a strain of 0.0012 when the interface debonds completely. Similar trends are seen for the combined loading (L2) in Figure 7(b), where material degradation is followed by a constant stiffness phase corresponding to locked state. The merit of representing the HCDM model in the PDCS is evident from the results of the nonproportional loading case (L3) in Figure 7(c). The PDCS representation results in a remarkable improvement of accuracy when compared to results in Figure 7(d), which are obtained without incorporation of PDCS. The stress Σ_{11} in this case keeps reducing in the second half of the loading. For the RVE (b) with the elliptical fiber, stress concentration at the major axis as shown in Figure 5(b) causes uneven debonding of the interface. This results in different behavior in different directions even for uniaxial tension as shown in Figures 8(a)–(c).

The debonded configuration of the RVE (c) with hexagonal arrangement of fibers with uniaxial loading is shown in Figure 5(c). The stress–strain plots in Figures 9(a)–(c) for this RVE under various loading histories show more gradual degradation than that for RVE (a) when compared with Figures 7(a)–(c). Figures 10(a)–(c) show macroscopic stress–strain plots
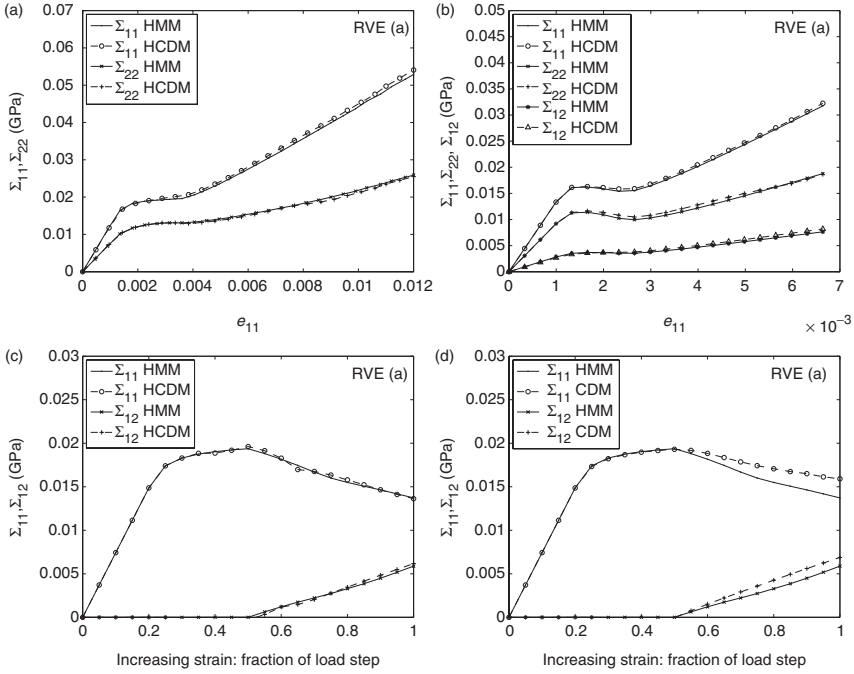
Figure 7. *Comparison of macroscopic stress–strain behavior obtained using HCDM and homogenized micromechanics (HMM) for RVE with a cylindrical fiber (Figure 2(a)), for load cases (a) L1, (b) L2, (c) L3, and (d) L3 without incorporation of PDCS.*

for the cross-ply composite RVE (d), shown in Figure 2(d). The Σ_{11} component of stress shows insignificant amount of softening for all three loading cases. This is because, for a tensile load in the x_1 direction, the major share of the load is supported by the fiber in x_1 direction. This fiber continues to support the tensile load even after debonding occurs in this fiber. Degradation of the elastic stiffness in the x_1 direction occurs mainly due to debonding at the interface of the fiber in the x_3 direction, which is not significant. On the other hand, the Σ_{22} plot for uniaxial tension (L1) case in Figure 10(a) shows the effect of considerable damage. The initial elastic response is followed by degradation, before stabilizing at a lower value of stiffness. There are two phases of rapid degradation corresponding to debonding of fibers in the x_3 and x_1 directions, respectively. The first is due to rapid separation of the fiber in the x_3 direction, whose axis is perpendicular to the loading direction (Figure 5(d)). Due to symmetry, degradation in the x_2 direction is equally affected by debonding of fibers in the x_1 and x_3 directions. When the RVE is subjected to tensile strain in the x_1 direction, imposed periodicity conditions in the three orthogonal
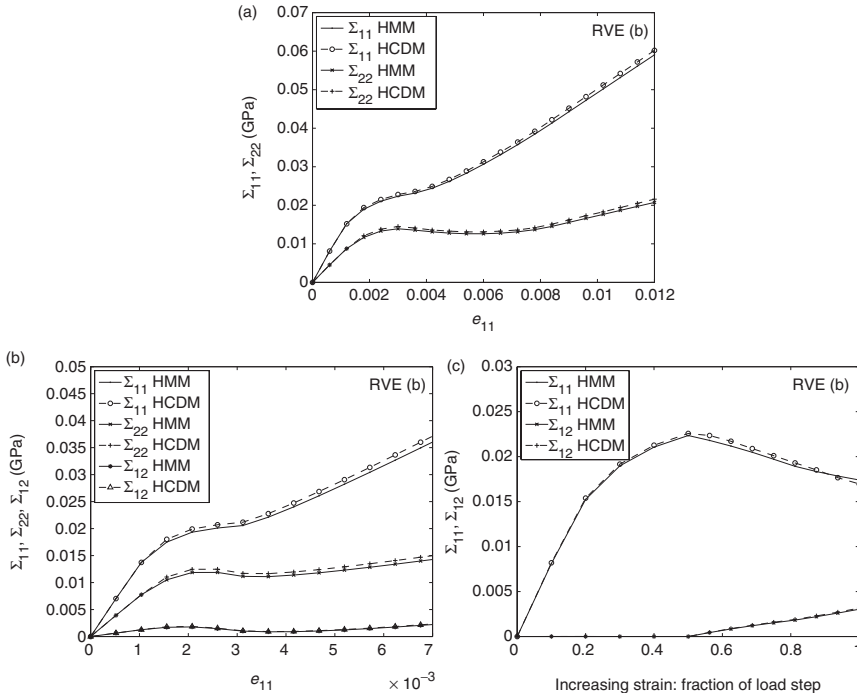
Figure 8. *Comparison of macroscopic stress–strain behavior obtained using HCDM and homogenized micromechanics (HMM) for RVE with an elliptical fiber (Figure 2(b)), for load cases (a) L1, (b) L2, and (c) L3.*

directions causes the material to experience tension in these directions. This is a consequence of Poisson's effect and the constraint to produce zero macroscopic strains in the x_2 and x_3 directions, which leads to interfacial separation of the fiber in x_3 direction. This second rapid degradation is due to this effect. Finally, when the two interfaces have debonded completely, the stress response in the x_2 direction corresponds to that of an RVE containing two voids. Similar behavior is also observed for the combined loading (L2) shown in Figure 10(b). The shear stress is seen to be affected more prominently by the debonding of fiber in x_1 direction.

The error in stress predicted by HCDM is attributed to the error in the functional representation of $\kappa'(W_d)$ and P'_{ijkl}, and the assumption of orthotropy. It is evident from the examples discussed that the material degradation and consequently the variation of damage parameters depend on the shape, distribution and orientation of the fibers in the RVE. This emphasizes the need for comprehensive 3D micromechanics-based continuum damage model for use in macroscopic analysis modules.
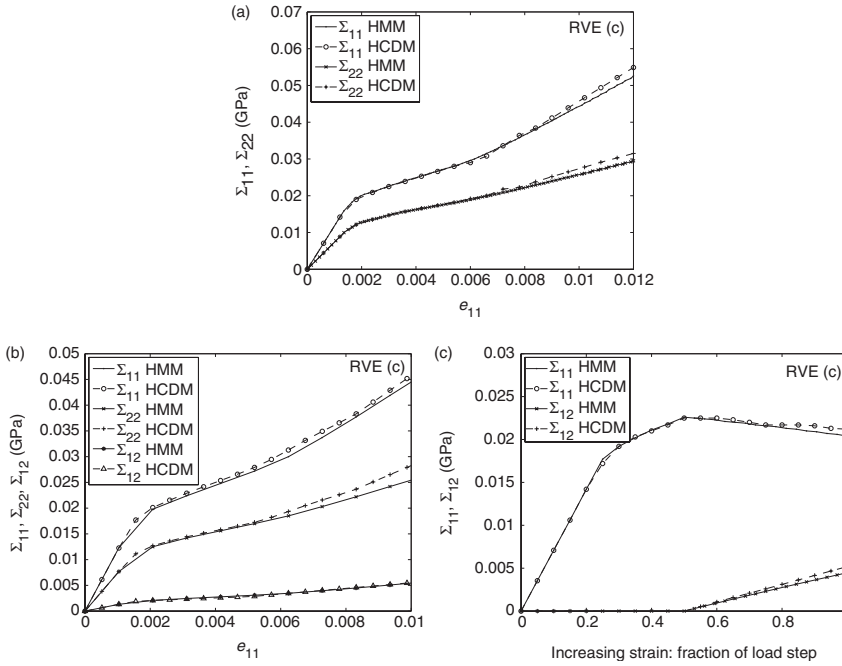
Figure 9. *Comparison of macroscopic stress–strain behavior obtained using HCDM and homogenized micromechanics (HMM) for RVE with hexagonal arrangement of fibers (Figure 2(c)), for load cases (a) L1, (b) L2, and (c) L3.*

MACRO–MICRO ANALYSIS OF A COMPOSITE STRUCTURE WITH THE HCDM MODEL

This section is intended to demonstrate the potential of HCDM model as a design tool for composite microstructures in structural applications by establishing a connection between macroscopic damage evolution and explicit microscopic failure mechanisms. Macroscopic structural simulations of damage evolution are conducted by the commercial FEM code ABAQUS (Abaqus, 2001) with the HCDM model incorporated in the user subroutine UMAT. Once calibrated and validated, the HCDM model for a given RVE can be used for macroscopic analysis using the stress update procedure explained in 'Implementation of the HCDM Model in a Macroscopic Analysis Module' section. A distinct advantage of the HCDM model over conventional macro–micro homogenization methods (Lene and Leguillon, 1982; Guedes and Kikuchi, 1991) is that the macroscopic analysis of large structures can be conducted very efficiently while preserving the effects of microstructural features.
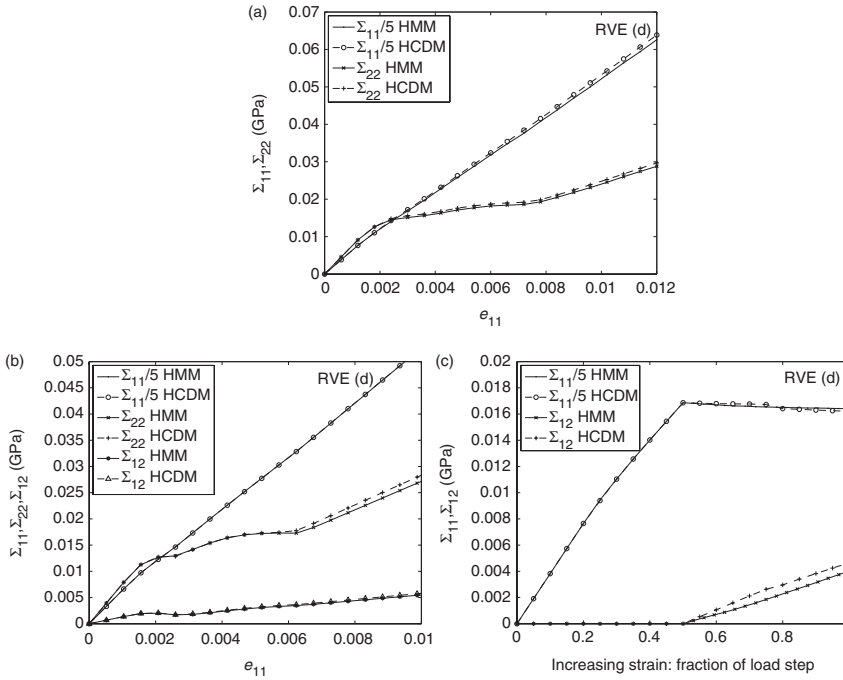
Figure 10. Comparison of macroscopic stress–strain behavior obtained using HCDM and homogenized micromechanics (HMM) for RVE with two perpendicular fibers (Figure 2(d)), for load cases (a) L1, (b) L2, and (c) L3.

The simulations involve a deformable composite projectile impactor, colliding with a rigid surface as shown in Figure 11. The impactor is cylindrical in shape with radius of 3.2 mm and length of 32.4 mm and is moving with initial velocity of 10 m/s. The impactors are assumed to be constituted of different microstructural RVEs, namely the RVEs (a), (b), (c), and (d) described in 'Numerical Examples for Validating the HCDM Model' section. The RVEs are oriented in the structure such that the local (RVE) 3-direction coincides with the global 2-direction of Figure 11. The macroscopic material behavior of the impactors are described by the calibrated HCDM models developed in 'Numerical Examples for Validating the HCDM Model' section. To account for the inertia effects, the simulations are conducted with ABAQUS/Explicit with the HCDM constitutive law incorporated in VUMAT. The density of epoxy matrix is assumed to be 750 kg/m^3 while that of steel fiber is 7800 kg/m^3 so that, for fiber volume fraction of 20%, the density of the aggregate is 2160 kg/m^3. The rigid surface and the projectile are modeled using continuum elements, and contact between projectile and rigid surface is assumed to be frictionless.
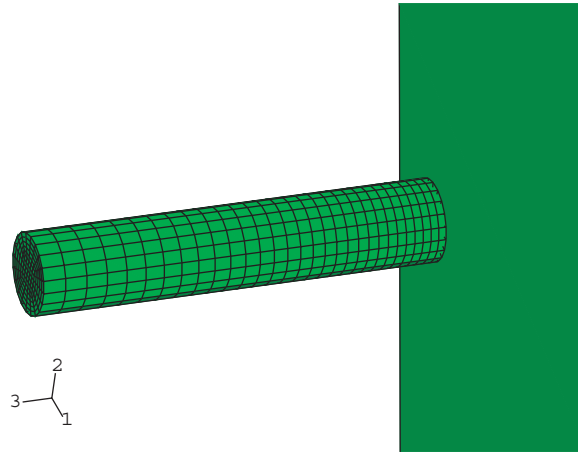
Figure 11. *Finite element model of a composite impactor colliding with a rigid surface.*
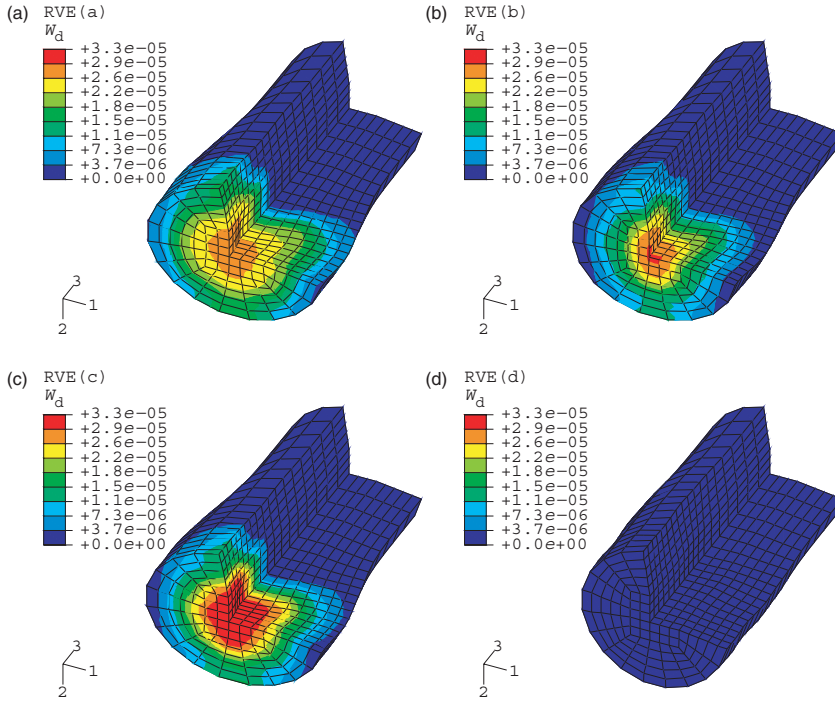
The total energy dissipated due to evolving damage (W_{d}) is plotted as a function of time in Figure 12 for the different composite microstructures. The composite impactor with RVE (a) undergoes maximum amount of damage while that with the cross-ply RVE (d) undergoes only nominal damage. For the composite with elliptical fiber reinforced RVE (b), the damage initiates earlier than that for RVEs (a) and (c). However, it accumulates at a lower rate, resulting in significantly lower value of W_{d} at the end of the simulation. Figures 13(a)–(d) and 14(a)–(d) show contour plots of energy dissipated W_{d} due to evolving damage at 2.2 and 5.0 μs, respectively for the different microstructures. The damage initiates near the periphery of the impactor head and then propagates towards the center of the head cross-section. It is observed that at $t = 2.2$ μs (Figure 13(a)–(d)), the maximum value of local accumulated W_{d} for composite with RVE (b) is significantly less than that for composite with RVE (a). Also, there is remarkable difference in the damage distribution for the two cases. In the latter case, damage is concentrated over a few elements while in the former case, it is more uniformly distributed about the center. This behavior may be attributed to the different shapes of the fibers. The composite impactor with RVE (c) shows lower value of maximum W_{d} than the composite with RVE (a); however, the distribution of damage is similar. At a later time $t = 5.0$ μs (Figure 14(a)–(d)), the maximum local W_{d} show a different trend. In this case, W_{d} is the highest for composite with RVE (c), followed by RVE (b), and then RVE (a). Different loading states affect the evolution of damage in each microstructural configuration in different ways resulting in different
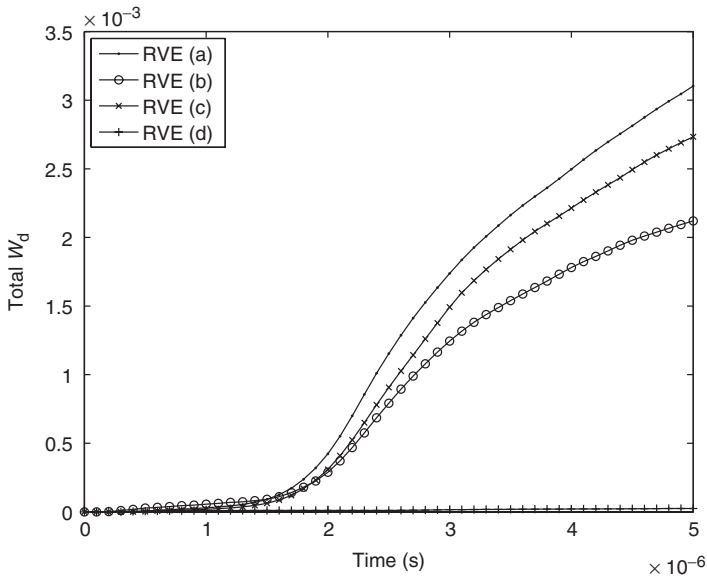
Figure 12. *Total energy dissipated (W_d) due to evolving damage in the composite impactor for four different microstructures.*
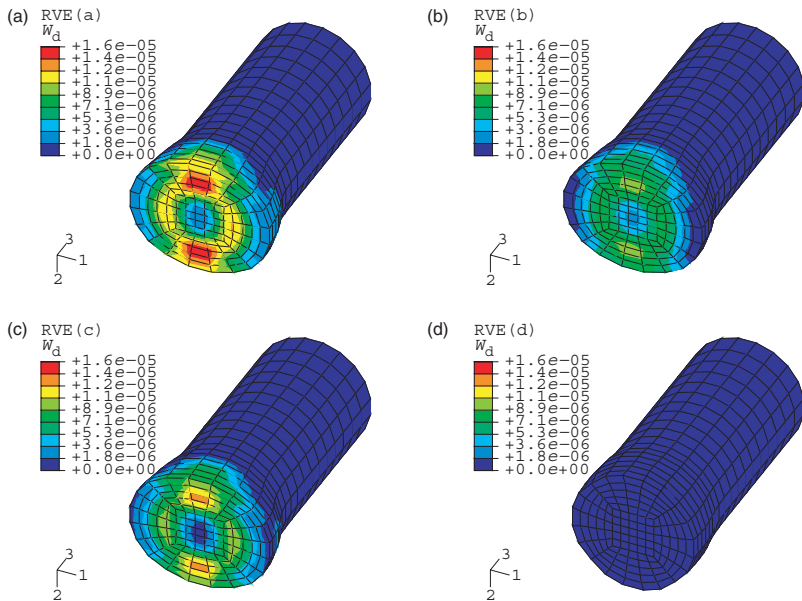
Figure 13. *Contour plots of energy dissipated (W_d) due to evolving damage for composite impactor with RVEs (a), (b), (c), and (d), at a time=2.2 μs.*

Figure 14. Contour plots of energy dissipated (W_d) due to evolving damage for composite impactor with RVEs (a), (b), (c), and (d), at time = 5.0 μs.

damaged behavior at various locations in the structure. However, the distribution of W_d is more uniform in composite with RVE (a), and hence the total W_d is more than for the other RVEs.

Time histories of the normal contact force at the impactor-rigid wall interface are compared in Figure 15(a)–(d). The problems for the four RVEs are solved with and without damage. The elastic stiffness tensor in the latter case is equal to the homogenized RVE stiffness with a perfect interface. The plots show that contact force rapidly reaches a peak value, reduces and stabilizes for a while and then gradually increases again. The later increase in contact force occurs earlier in the cross-ply composite. Stress waves generated during impact propagate away from the center of impactor head towards the periphery. Also the waves propagate towards the back end of the impactor. Due to material orthotropy, the waves propagate at different speeds in different directions. The waves get reflected from the boundaries and interact with each other, causing the later increase in contact force. This occurs earlier in cross-ply composite because of higher
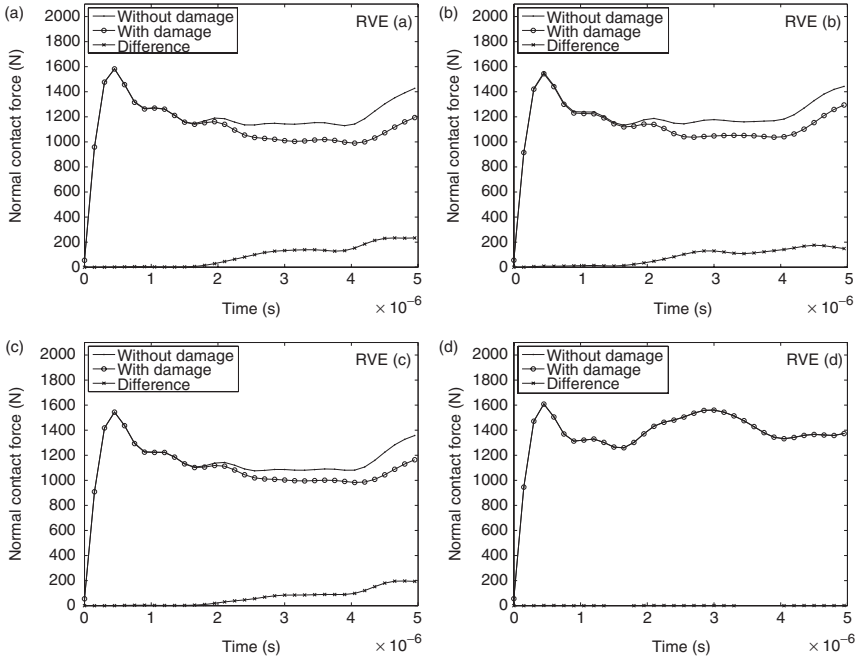
Figure 15. *Comparison of the interfacial contact force during impact with and without interfacial damage for composite impactors with RVEs (a), (b), (c), and (d).*

wave speeds. For the impactors with RVEs (a), (b), and (c), the contact force with and without damage are concurrent until damage initiation, after which, the contact force with damage accumulation is lower. The difference between the two curves increases as more and more damage accumulates, indicating reduction in the load carrying capacity of the material. The difference is negligible for the cross-ply composite owing to negligible damage accumulation.

Finally, the homogenization method allows for the assessment of stress–strain and damage evolution in the microstructural RVE, subject to a given macroscopic strain history. Figure 16(a)–(d) show the stress σ_{11} contour plots in the microstructural RVEs at a point on the face of the impactor. At this point, the macroscopic stress evolution predicted by HCDM model is compared with the homogenized stress obtained from the microstructural RVE analysis subjected to macroscopic strain history. The comparison is demonstrated in the Figure 17(a)–(d). Excellent agreement between the HCDM and the homogenized micro-scale distributions confirm the robustness of the HCDM model.
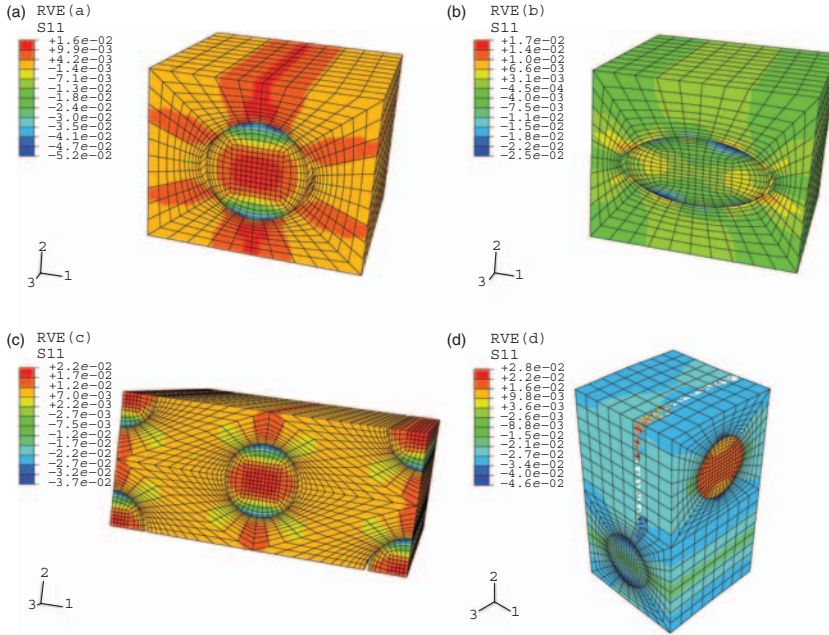
Figure 16. *Contour plots of the microscopic stress (σ_{11}) in the RVE, at a macroscopic point on the head of the composite impactor for RVEs (a), (b), (c), and (d).*

The evolution of stresses in Figure 17(a)–(c) show change from initial negative region to positive values. After that, the stress Σ_{22} undergoes fluctuations while Σ_{11} remains positive till the end of the simulation. The initial negative region corresponds to the compressive stress waves generated due to impact. As these compressive waves propagate into the impactor, and the waves on the contact surface get reflected from the periphery, the stresses become tensile. Because of the strong material anisotropy, the Σ_{22} waves undergo multiple reflections, generating alternate tensile and compressive waves going into the impactor. However, this stress component does not contribute to damage significantly as it is along the direction of the fibers. The Σ_{33} (not shown in the figures) remains negative throughout the simulation and is inconsequential to the damage. Also, the shear component Σ_{12} remains small. Therefore, the damage accumulation at this material point is mainly affected by evolution of Σ_{11}. In case of cross-ply RVE (d) (Figure 17(d)), both Σ_{11} and Σ_{22} are along fiber directions and Σ_{33} (not shown) is negative. Hence, only nominal damage is accumulated in this case.
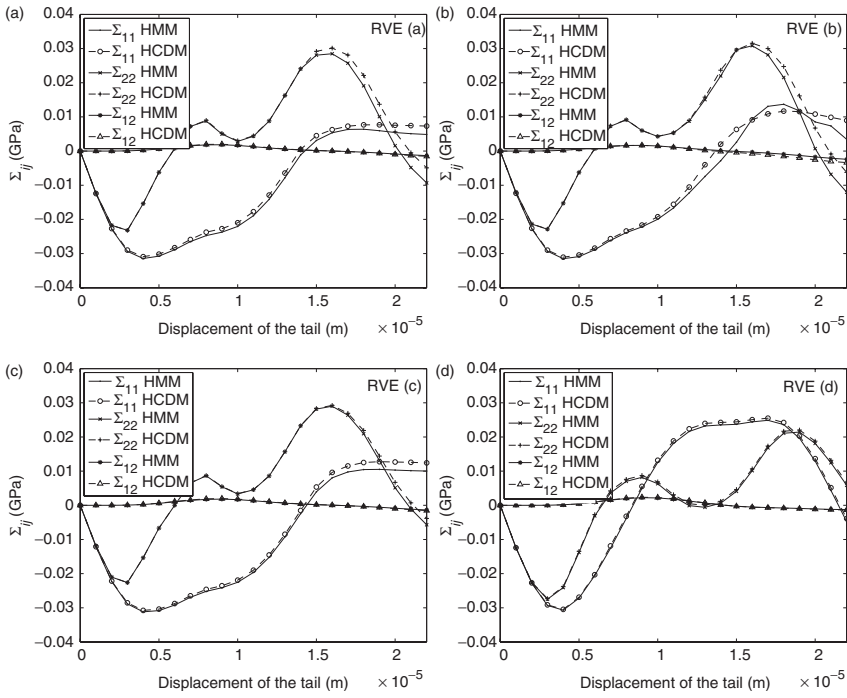
Figure 17. *Comparison of stress evolution predicted by HCDM model and the homogenized micromechanics (HMM) at a macroscopic point on the head of the composite impactor for RVEs (a), (b), (c), and (d).*

CONCLUSIONS

An accurate and computationally efficient 3D homogenization-based continuum damage mechanics model (HCDM) is developed in this paper for fiber reinforced composites undergoing interfacial debonding. The HCDM model represents orthotropic behavior in the PDCS and uses a fourth order damage tensor which characterizes the stiffness as an internal variable. The model is found to accurately predict damage behavior for a wide range of proportional and nonproportional loading. The orientation of the principal damage axes can change significantly with the evolution of damage, depending on the load history. The effect is particularly pronounced for nonproportional load-strain histories. This effect is accounted for by expressing the damage evolution laws in the PDCS. Functional forms of various damage parameters κ', P'_{ijkl} are developed in terms of the strain invariants I_1, J_2, and J_3 and damage dissipation energy W_d to express

variation of damage variables with the evolving damage. Parameters are calibrated by performing micromechanical RVE analysis for a few imposed strain histories. The functional forms of the parameters overcome the serious limitations of constant damage parameters that are conventionally assumed in CDM models. Numerical experiments clearly demonstrate that constant parameter damage laws are not able to accurately predict the damage behavior. The assumption of orthotropy of damage laws in the PDCS is found to yield reasonably good accuracy. The model's robustness is evident from the good agreement between HCDM and HMM response of different RVEs for a variety of loading paths.

The HCDM model is a very effective tool in making macroscopic damage predictions in structures with explicit reference to the microstructural composition. This capability is largely lacking in the literature. The macroscopic behavior is sensitive to the shape, spatial arrangement as well as orientation of the fibers. Therefore, different microstructural configurations may be suitable at different locations in the structure depending on the loading conditions. The HCDM model can hence be used in a material design framework to enhance the mechanical properties of structures/components by optimizing microstructural configurations and compositions.

The present model however has some limitations that are currently being investigated by the authors. The model assumes the existence of an RVE microscopic periodicity that yield uniform macroscopic response. As shown in Swaminathan et al. (2006a), the RVE continuously evolves in size with the evolution of microscopic damage. Continuous adjustments are needed for their incorporation in damage models. Higher order size dependent damage models with changing length scale parameters are currently being looked into to overcome this shortcoming. A second limitation is that although the microstructural model accounts for crack opening and closing, it is not explicitly accounted for in the macroscopic model. Specifically, the present work does not take into account the effect of reverse or cyclic loading. A new HCDM model that explicitly accounts for crack closure effects during cyclic loading is currently being developed by the authors, and will be reported soon.

ACKNOWLEDGMENTS

REFERENCES

Abaqus (2001). *Users Manual*, Hibbit, Karlsson and Sorensen, Inc., Pawtucket, USA.

Allix, O. and Hild, F. (2002). *Continuum Damage Mechanics of Materials and Structures*, Elsevier, Oxford, UK.

Camacho, G.T. and Ortiz, M. (1996). Computational Modeling of Impact Damage in Brittle Materials, *Int. J. Solids Struct.*, **33**: 2899–2938.

Carol, I., Rizzi, E. and Willam, K. (1994). A Unified Theory of Elastic Degradation and Damage based on a Loading Surface, *Int. J. Solids Struct.*, **31**(20): 2835–2865.

Chaboche, J.L. (1981). Continuum Damage Mechanics: A Tool to Describe Phenomena before Crack Initiation, *Nuclear Engrg. Design*, **64**: 233–247.

Chaboche, J.L., Kruch, S. and Pottier, T. (1998). Micromechanics Versus Macromechanics: A Combined Approach for Metal Matrix Composite Constitutive Modeling, *Eur. J. Mech. A/Solids*, **17**: 885–908.

Chan, L.C., Cheng, C.H., Jie, M. and Chow, C.L. (2005). Damage-based Formability Analysis for TWBs, *Int. J. Damage Mech.*, **14**(1): 96–83.

Chandra, N., Li, H., Shet, C. and Ghonem, H. (2002). Some Issues in the Application of Cohesive Zone Models for Metal-ceramic Interface, *Int. J. Solids Struct.*, **39**: 2827–2855.

Choi, J. and Tamma, K.K. (2001). Woven Fabric Composites – Part I: Prediction of Homogenized Elastic Properties and Micromechanical Damage Analysis, *Int. J. Numer. Meth. Engrg.*, **50**: 2285–2298.

Chow, C. and Wang, J. (1987). An Anisotropic Theory of Elasticity for Continuum Damage Mechanics, *Int. J. Frac.*, **20**: 381–390.

Chow, C., Yang, X.J. and Edmund, C. (2001). Viscoplastic Constitutive Modeling of Anisotropic Damage under Nonproportional Loading, *J. Engng. Mater. Tech.*, **123**: 403–408.

Cordebois, J. and Sidoroff, F. (1982). Anisotropic Damage in Elasticity and Plasticity, *J. Mech. Theor. Appl.*, 45–60.

Costanzo, F., Botd, J.G. and Allen, D.H. (1995). Micromechanics and Homogenization of Inelastic Composite Materials with Growing Cracks, *Eur. J. Mech. Phy. Solids*, **44**(3): 333–370.

Desmorat, R., Ragueneau, F. and Pham, H. (2007). Continuum Damage Mechanics for Hysteresis and Fatigue of Quasi-brittle Materials and Structures, *Int. J. Numer. Anal. Meth. Geomech.*, **31**: 307–329.

Feyel, F. and Chaboche, J.L. (2000). FE2 Multiscale Approach for Modelling the Elastoviscoplastic behaviour of Long Fibre SiC/Ti Composite Materials, *Comput. Meth. Appl. Mech. Engrg.*, **183**: 309–330.

Fish, J., Yu, Q. and Shek, K. (1999). Computational Damage Mechanics for Composite Materials based on Mathematical Homogenization, *Int. J. Numer. Meth. Engrg.*, **45**: 1657–1679.

Ghosh, S., Bai, J. and Raghavan, P. (2007). Concurrent Multi-level Model for Damage Evolution in Microstructurally Debonding Composites, *Mech. Mater.*, **39**(3): 241–266.

Ghosh, S., Lee, K. and Raghavan, P. (2001). A Multi-level Computational Model for Multi-scale Damage Analysis in Composite and Porous Materials, *Int. Jour. Solids Struct.*, **38**(14): 2335–2385.

Ghosh, S., Ling, Y., Bhaskar, M. and Ran, K. (2000). Interfacial Debonding Analysis in Multiple Fiber Reinforced Composites, *Mech. Mater.*, **32**: 561–591.

Guedes, J.M. and Kikuchi, N. (1991). Preprocessing and Post Processing for Materials based on the Homogenization Method with Adaptive Finite Element Methods, *Comp. Meth. Appl. Mech. Engng.*, **83**: 143–198.

Hill, R. (1948). A Theory of the Yielding and Plastic Flow of Anisotropic Metals, *Proceedings of Royal Society of London*, **A193**: 281–297.

Ju, J.W., Ko, Y.F. and Ruan, H.N. (2006). Effective Elastoplastic Damage Mechanics for Fiber-reinforced Composites with Evolutionary Complete Fiber Debonding, *Int. J. Damage Mech.*, **15**(3): 237–265.

Kachanov, L.M. (1987). *Introduction to Continuum Damage Mechanics*, Dordrecht, Boston, M. Nijhoff, Boston.

Kouznetsova, V., Brekelmans, W.A.M. and Baaijens, F.P.T. (2001). An Approach to Micro-macro Modeling of Heterogeneous Materials, *Computational Mech.*, **27**: 37–48.

Krajicinovic, D. (1996). *Damage Mechanics*, Elsevier, Amsterdam, Netherlands.

Ladeveze, P. (2002). An Anisotropic Damage Theory with Unilateral Effects: Applications to Laminates and to Three- and Four-dimensional Composites, In: Allix, O. and Hild, F. (eds), *Continuum Damage Mechanics of Materials and Structures*, Elsevier, Oxford, UK, Vol. 1, pp. 205–233.

Lemaitre, J. and Chaboche, J.L. (1990). *Mechanics of Solids*, Cambridge University Press, Cambridge, UK.

Lene, F. and Leguillon, D. (1982). Homogenized Constitutive Law for a Partially Cohesive Composite Material, *Int. J. Solids Struct.*, **18**(5): 443–458.

Li, S. and Ghosh, S. (2004). Debonding in Composite Microstructures with Morphologic Variations, *International Journal of Computational Methods*, **1**(1): 21–149.

Massart, T.J., Peerlings, R.H.J. and Geers, M.G.D. (2007). Structural Damage Analysis of Masonary Walls using Computational Homogenization, *Int. J. Damage Mech.*, **16**(2): 199–226.

Matzenmiller, A., Lubliner, J. and Taylor, R.L. (1995). A Constitutive Model for Anisotropic Damage in Fiber-composites, *Mech. Mater.*, **20**: 125–152.

Murakami, S. (1988). Mechanical Modeling of Material Damage, *J. Appl. Mech.*, **55**: 280–286.

Needleman, A. (1990). An Analysis of Decohesion Along an Imperfect Interface, *Int. J. Fracture*, **42**: 21–40.

Needleman, A. (1992). Micromechanical Modeling of Interfacial Decohesion, *Ultramicroscopy*, **40**: 203–214.

Nemat-Nasser, S. and Hori, M. (1999). *Micromechanics : Overall Properties of Heterogeneous Materials*, North-Holland, Elsevier, Amsterdam, Netherlands.

Ortiz, M. (1985). A Constitutive Theory for the Inelastic behavior of Concrete, *Mech. Mater.*, **4**: 67–93.

Ortiz, M. and Pandol, A. (1999). Finite-deformation Irreversible Cohesive Element for Three-dimensional Crack-propagation Analysis, *Int. Jour. Numer. Meth. Engng.*, **44**: 1267–1282.

Pellegrino, C. Galvanetto, U. and Schrefler, B.A. (1999). Numerical Homogenization of Periodic Composite Materials with Non-linear Material Components, *Int. J. Numer. Meth. Engrg.*, **46**: 1609–1637.

Raghavan, P. and Ghosh, S. (2004). Concurrent Multi-scale Analysis of Elastic Composites by a Multi-level Computational Model, *Comput. Meth. Appl. Mech. Engng.*, **193**(6–8): 497–538.

Raghavan, P. and Ghosh, S. (2005). A Continuum Damage Mechanics Model for Unidirectional Composites Undergoing Interfacial Debonding, *Mech. Mater.*, **37**(9): 955–979.

Segurado, J. and Llorca, J. (2002). A Numerical Approximation to the Elastic Properties of Sphere-reinforced Composites, *J. Mech. Phy. Solids*, **50**: 2107–2121.

Sharma, P., Dasgupta, A. and Cuddalorepatta, G. (2005). The Connection between Microstructural Damage Modeling and Continuum Damage Modeling for Eutectic SnPb Solder Alloys, *Int. J. Damage Mech.*, **14**(4): 343–363.

Simo, J.C. and Ju, J.W. (1987). Strain and Stress-based Continuum Damage Models, Part I: Formulation, *Int. J. Solids Struct.*, **23**(7): 821–840.

Swaminathan, S., Ghosh, S. and Pagano, N. J. (2006a). Statistically Equivalent Representative Volume Elements for Composite Microstructures, Part I: Without Damage, *J. of Comp. Mater.*, **40**(7): 583–604.

Swaminathan, S., Pagano, N.J. and Ghosh, S. (2006b). Analysis of Interfacial Debonding in Three-dimensional Composite Microstructures, *J. Engng. Mater. Tech.*, **128**: 96–106.

Voyiadjis, G.Z. and Kattan, P.I. (1992). A Plasticity-damage Theory for Large Deformation of Solids. Part I: Theoretical Formulation, *Int. J. Engrg. Sci.*, **30**(9): 1089–1108.

Voyiadjis, G.Z. and Kattan, P.I. (1996). On the Symmetrization of the Effective Stress Tensor in Continuum Damage Mechanics, *J. Mech. Beha. Mater.*, **7**(2): 139–165.

Voyiadjis, G.Z. and Kattan, P.I. (2006). *Advances in Damage Mechanics: Metals and Metal Matrix Composites with an Introduction to Fabric Tensors*, Elsevier, Oxford, UK.

Voyiadjis, G.Z., Kattan, P.I. and Taqieddin, Z.N. (2007). Continuum Approach to Damage Mechanics of Composite Materials with Fabric Tensors, *Int. J. Damage Mech.*, **16**(3): 301–330.

Wriggers, P., Zavarise, G. and Zohdi, T.I. (1998). A Computational Study of Interfacial Debonding Damage in Fibrous Composite Materials, *Compu. Mater. Sci.*, **12**: 39–56.